Crumpled reduced graphene oxide conformally encapsulated hollow V$_2$O$_5$ nano/microsphere achieving brilliant lithium storage performance

Bo Yan [a,b,c], Xifei Li [a,b,*], Zhimin Bai [c,**], Yang Zhao [a,b,d], Lei Dong [a,b], Xiaosheng Song [a,b,c], Dejun Li [a,b], Craig Langford [d], Xueliang Sun [d,a,b,***]

[a] Energy & Materials Engineering Centre, College of Physics and Materials Science, Tianjin Normal University, Tianjin 300387, China
[b] Tianjin International Joint Research Centre of Surface Technology for Energy Storage Materials, Tianjin 300387, China
[c] Beijing Key Laboratory of Materials Utilization of Nonmetallic Minerals and Solid Wastes, National Laboratory of Mineral Materials, School of Materials Science and Technology, China University of Geosciences, Beijing 100083, China
[d] Nanomaterials and Energy Lab, Department of Mechanical and Materials Engineering, University of Western Ontario, London, Ontario, Canada N6A 5B9

ARTICLE INFO

ABSTRACT

It has remained a challenge to develop a facile and scalable approach to synthesize high-energy lithium-ion battery (LIB) electrode materials with excellent rate capabilities and prominent cycling stabilities for their applications in new generation energy storage devices. In this study, for the first time, we report a crumpled reduced graphene oxide (cG) encapsulated three-dimensional (3D) hollow vanadium pentoxide (V$_2$O$_5$) nano/microspheres fabricated by one-step solvothermal treatment followed by subsequent annealing. This rapid and effective synthesis method is environmental friendly and economically beneficial without involving costly organic vanadium sources, tedious operation, or sophisticated equipment. Remarkably, the desired cG-encapsulated V$_2$O$_5$ composite contains 5 wt% reduced graphene oxide (rGO), yet exhibits outstanding rate capacities and cycling stabilities. This product can deliver reversible capacities of 289 mA h g^{-1} at 100 mA g^{-1} and 163 mA h g^{-1} at 5000 mA g^{-1} (492 W h kg^{-1} and 9840 W kg^{-1}), as well as a capacity retention of about 94% after 200 cycles at 2000 mA g^{-1} in the potential range between 2.0 V and 4.0 V (vs. Li/Li$^+$). Furthermore, the unique structural feature and typical formation mechanism of the designed materials are clarified based on multiple experimental results. More commendably, a chain of solid powders had been successfully encapsulated using this scalable reaction system. It is expected that this versatile approach will facilitate the applications of cG, and provide a novel avenue to create more fascinating rGO-based functional materials.

1. Introduction

Lithium ion batteries (LIBs) have been regarded as one of the most promising candidates for applications in the coming era of electric and hybrid vehicles with the potential to lower fossil fuels consumption and reduce greenhouse gas emissions [1–4]. Nonetheless, to meet the constantly increasing demands of new generation energy storage devices such as portable electronic devices, electric vehicle propulsion, and grid-scale energy storage, high energy density rechargeable battery electrode materials with excellent rate capabilities and prominent cycling stabilities have attracted considerable research interests worldwide [5,6].

Being a well-known transition-metal oxide with multiple valence states, vanadium pentoxide (V$_2$O$_5$) has been extensively studied as one of the most promising LIB cathode materials due to its unique advantages such as its rich abundance, ease of synthesis, being relatively safer, and high specific capacity [7–11]. V$_2$O$_5$ consists of a layer structure stacked along the c-axis of the orthorhombic structure, as shown in the Supplementary Fig. S1a. Each layer is in turn made up of VO$_5$ square pyramids sharing edges and corners, and the layers are bonded together only by the interaction of weak van der Waals forces. Therefore, this structure easily undergoes multiple phase transitions, such as α, ε, δ, γ, and

* Corresponding author at: Energy & Materials Engineering Centre, College of Physics and Materials Science, Tianjin Normal University, Tianjin 300387, China. Tel.: +86 22 23766526; fax: +86 22 23766503.
** Corresponding author.
*** Corresponding author.
E-mail addresses: xfli2011@hotmail.com (X. Li), zhimibai@cugb.edu.cn (Z. Bai), xsun@eng.uwo.ca (X. Sun).

ω phases, relying on the depth of Li intercalation (x) [12]. The α-phase $Li_xV_2O_5$ ($x < 0.01$) and ε-phase $Li_xV_2O_5$ ($0.35 < x < 0.7$) have similar structure with the un-intercalated V_2O_5, but result in weak wrinkling of V_2O_5 layers [13]. With further Li intercalation, the δ-phase $Li_xV_2O_5$ ($0.7 < x < 1$) has more corrugated V_2O_5 layers. Meanwhile, the c parameter is doubled due to the shift of the V_2O_5 layers (see Supplementary Fig. S1b). When lithiated further, the irreversible structural variation to γ-phase $Li_xV_2O_5$ ($1 < x < 2$) appears. Fig. S1 clearly reveals the difference in crystal structures of δ-and γ-V_2O_5 phases. The layer wrinkling of γ-V_2O_5 becomes more evident than that in δ-phase [13]. A further deep discharge to $x > 2$ results in the irreversible formation of ω-$Li_xV_2O_5$ with a rock salt type structure, where the Li^+ migration will be very tardy [12]. As a result, the theoretical capacity and structural stability of V_2O_5 highly depends on the depth of the Li intercalation, *viz.*, the potential window of charge/discharge measurement. Normally, when V_2O_5 is employed as a cathode material in the potential range of 2.0–4.0 V (*vs.* Li/Li^+), its theoretical capacity reaches about 294 mA h g^{-1} corresponding to the two Li intercalation/deintercalation mechanisms, much higher than those of conventional $LiMn_2O_4$ (148 mA h g^{-1}) [14], $LiCoO_2$ (140 mA h g^{-1}) [15], or $LiFePO_4$ (170 mA h g^{-1}) [16]. Nevertheless, the high specific capacity/energy has not been realized in practical LIB applications because of four drawbacks, as follows: (1) poor electrical conduction, (2) irreversible phase transitions upon deep discharge, (3) vanadium dissolution, and (4) fast increased charge transfer resistance upon cycling [12,17–21].

To mitigate the aforementioned intrinsic problems, decreasing their particle size to the nanoscale level is generally believed to be one of the most effective approaches due to the shorter transport lengths for both electrons and Li ions, larger electrode/electrolyte contact area, and higher electrochemical reaction activity and reversibility of the nanostructures for Li intercalation/deintercalation [22–25]. Along this direction, the nanostructured V_2O_5 with diverse morphologies including nanorods [20,21], nanofibers [22], nanobelts [23], nanosheets [24], and porous micro-spheres [11,25] has already been investigated to realize Li battery application. Furthermore, it is noteworthy that the introduction of electrically conductive materials, such as CNTs [26], conductive polymers [27], and reduced graphene oxide (rGO) [17,28,29], into these nanostructured V_2O_5 materials can further improve the battery properties. Among numerous conductive matrixes, rGO is preferable to replace other matrixes owing to its extraordinary properties including high electrical conductivity, unusual mechanical strength, and large specific surface area [30,31]. As a consequence, a number of rGO/V_2O_5 nanocomposites have been designed to idealize the electrochemical performance of the active materials, and have yielded a variety of notable results [17,28,29,32–36]. For example, Liu et al. have recently constructed V_2O_5 nanoribbons incorporated rGO sheets hybrid cathode materials that combined the effects of improving electronic conduction, Li-ion diffusion, and structural reversibility [29]. Despite the achieved high charge/discharge rates, these previous studies utilized costly organic vanadium source [32–34], tedious operation [28,29,35], or sophisticated equipment [17,36], in the synthesis process, which may be difficult to achieve large-scale applications. More importantly, the resulting V_2O_5 was only in a rough manner to combine with rGO, such as anchoring onto the rGO surface [17,29,32–34], sandwiching between rGO [28], and uneven hybrid or mixture with rGO [35]. There is still considerable room for improving the structure and properties of these composites for LIBs. Coincidentally, Zhao's group recently reported a cG-encapsulated 3D Ni_3S_2/Ni electrode with self-adaptive strain-relaxation via a multi-step process. The nanocomposites exhibited extraordinary electrochemical performance originating from the conformal wrapping of active materials by elastic rGO [37]. However, due to the lack of the

appropriate synthetic methods, the cG-encapsulated electroactive materials were seldom previously reported to the best of our knowledge [37–39]. Therefore, there is still a great desire as well as challenge to develop an easy, effective, and extensible approach for the design and synthesis of this kind of material, allowing the facilitation of the applications of cG.

Herein, we present a facile and rapid approach to realize cG-encapsulated 3D porous V_2O_5 nano/microsphere for the first time. This high-efficiency synthetic method involves a one-step solvothermal synthesis subsequently followed by low-temperature annealing. The whole process is environmentally friendly and economically beneficial. Noticeably, when the obtained materials serve as a cathode material for LIBs, the resulting electrodes exhibit superior cycling stability and rate capacities, due to the simultaneous improvement of the above-mentioned four major drawbacks. Even more remarkable, a series of solid powder materials had been successfully encapsulated using this scalable reaction system, further highlighting the practicality of this versatile method. It is expected that such finding will open up the possibility of producing more novel rGO-based functional materials.

2. Experimental section

2.1. Materials preparation

Graphite oxide (GO) was fabricated by the modified Hummers method, as previously reported by our group [40]. The obtained GO was ground into fine powder. This purified powder was dispersed in ethylene glycol by ultrasonic cell disruption for 20 min to form a 2.0 mg mL^{-1} brown solution. Secondly, the commercial V_2O_5 (0.3 g) and $H_2C_2O_4 \cdot 2H_2O$ in a molar ratio of 1:3 was dissolved in 30 mL of deionized H_2O under vigorous stirring at 70 °C for 1 h until a clear dark blue VOC_2O_4 solution (0.11 M) was formed [41]. Then 3 mL of the prepared VOC_2O_4 solution and 5 mL of the prepared GO dispersion were added into a 50 mL Teflon container pre-filled with 30 mL of butanol [11]. After stirring for 30 min, the container was sealed in a steel autoclave and kept in an electrical oven at 200 °C for 8 h. After cooling down naturally, the precipitate was collected by vacuum filtration and washed with pure ethanol several times. Finally, the cG-encapsulated V_2O_5 was obtained by sintering the dried precipitate in air at 350 °C for 2 h with a heating rate of 5 °C min^{-1}. For comparison, the changed amounts (0 mL, 2 mL) of the prepared GO dispersion were used in the above-mentioned experimental system without adjusting other conditions to study their effect on the morphology, structure, and performance of the final V_2O_5.

2.2. Materials characterization

Field-emission scanning electron microscopy (FE-SEM) coupled with energy dispersive spectroscopy (EDS) images were taken using a Hitachi SU8010 field-emission scanning electron microscope. The microstructure and micro-area chemical composition of the samples were verified using a transmission electron microscopy (TEM, JEOL JEM-3000F) with an accelerating voltage of 200 kV. X-ray powder diffraction (XRD) was performed on a Bruker AXS D8 advance X-ray diffractometer at the 2θ range of 10–70° using Cu Kα radiation ($\lambda = 1.5405$ Å). Traces software in combination with the Joint Committee on Powder Diffraction Standards (JCPDS) powder diffraction files was employed to identify the material phases. The amount of graphene in the final product was estimated using a thermogravimetric analysis (TGA, Pyris Diamond6000 TG/DTA, PerkinElmer) from 25–500 °C at 5 °C min^{-1} under air atmosphere. Fourier transform infrared (FTIR) spectra were collected on a IRAffinity-1 FTIR spectrometer (SHIMADZU) by using pressed KBr pellets. Raman

analysis was conducted on a confocal Micro Raman Spectrometer with LabRAM HR800 system (HORIBA) in the range of 200–1800 cm^{-1}. X-ray photoelectron spectroscopy (XPS, VG ESCA-LAB MK II) was carried out with Al Kα radiation as the X-ray source for excitation to determine the elemental information of the obtained materials.

2.3. Battery assembly and performance measurements

The working electrode slurry was fabricated by dispersing 70% active materials, 20% acetylene black, and 10% polyvinylidene fluoride binder in N-methyl pyrrolidinone solvent. The resultant slurry was spread uniformly on an aluminum foil, and dried overnight in a vacuum at 80 °C. The 2032 typed coin cells were assembled in an Ar-filled dry glovebox using lithium foil as negative electrode, porous polypropylene as the separator, and 1 M LiPF$_6$ in ethylene carbonate, dimethyl carbonate, and ethylene methyl carbonate (1:1:1 by volume) as the electrolyte. Galvanostatic charge/discharge tests with various current densities were performed using a Land battery testing system (LANHE CT2001A) in the voltage range of 2.0–4.0 V (vs. Li/Li$^+$). Cyclic voltammograms (CV) was collected using a VersaSTAT 4 electrochemical workstation at a scan rate of 0.1 mV s^{-1}. An AC amplitude of 5 mV was employed to measure electrochemical impedance spectroscopy (EIS) within the frequency range from 0.01 Hz to 100 kHz.

3. Results and discussion

3.1. Morphology and structure characterization

All the powder samples were prepared by designing a solvothermal-precursor method with a subsequent heat treatment. Specifically, using VOC$_2$O$_4$ and GO-ethylene glycol suspension as the raw materials, and butanol as the reaction solvent, VO$_2$ precursor was generated by hydrolyzing VOC$_2$O$_4$ [11,41]. Meanwhile, the graphene oxide was effectively reduced in this process. The obtained VO$_2$ materials with the addition of 0 mL, 2 mL, and 5 mL of the prepared GO-ethylene glycol dispersion were denoted as VO$_2$-P, VO$_2$-G, and VO$_2$-cG, respectively. Subsequent annealing of VO$_2$ intermediate phase in air led to the formation of V$_2$O$_5$ and the mild oxidation of rGO. The final sintering products with the addition of 0 mL, 2 mL, and 5 mL of the prepared GO-ethylene glycol dispersion were denoted as V$_2$O$_5$-P, V$_2$O$_5$-G, and V$_2$O$_5$-cG, respectively. Fig. 1 shows the low- and high-magnification FESEM images of the obtained precursors for VO$_2$-P, VO$_2$-G, and VO$_2$-cG, respectively. One can clearly observe in Fig. 1 that all of the VO$_2$ precursors presented regular spherical structure. Importantly, the particle sizes and micro-surface morphologies of the resultant VO$_2$ nano-microspheres were obviously influenced by the dosage of GO-ethylene glycol dispersion. To be specific, as shown in Fig. 1a, the VO$_2$-P possessed a relatively wide size distribution and rough

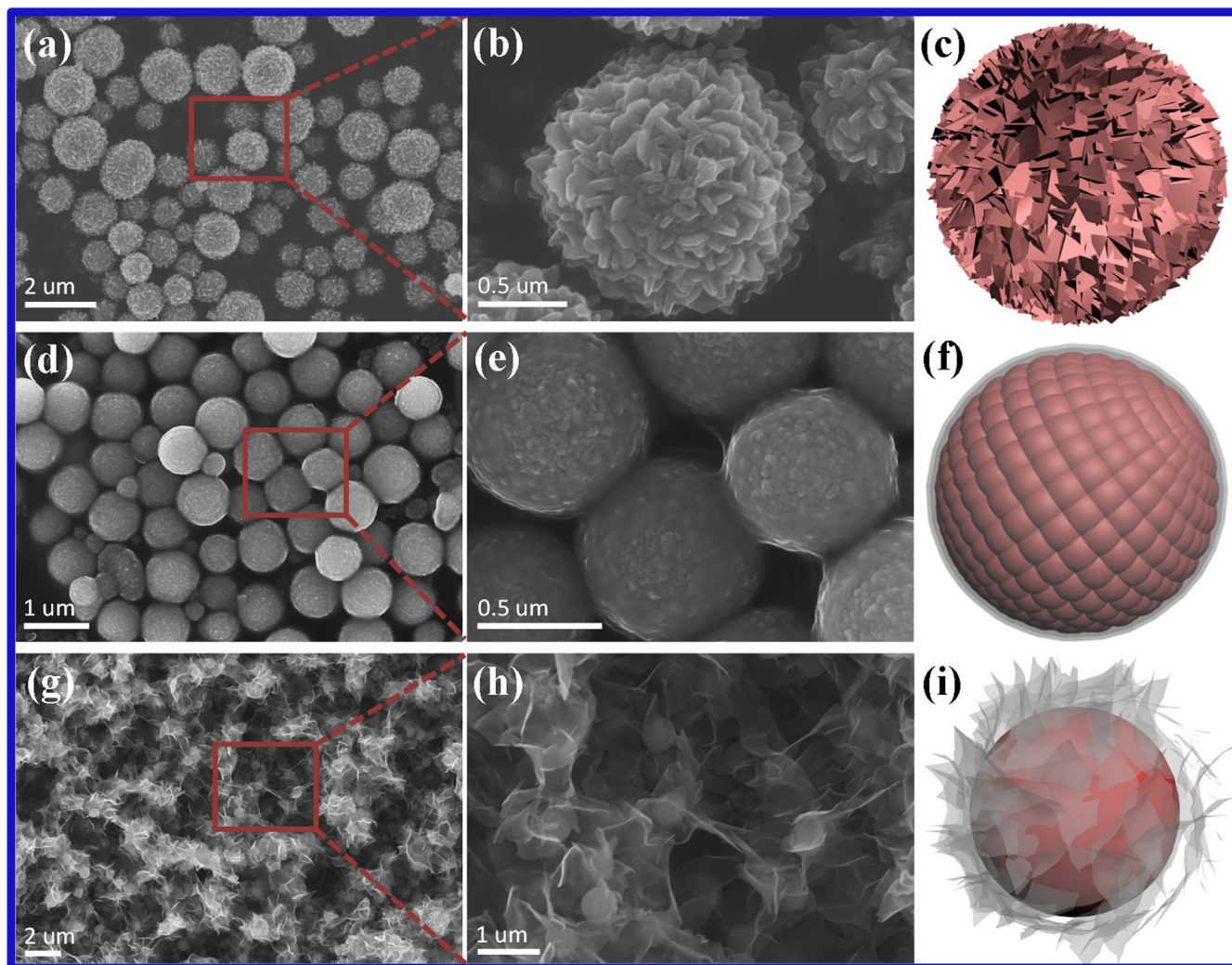**Fig. 1.** Low- and high-magnification FESEM images of the obtained precursors: (a andb) VO$_2$-P, (d and e) VO$_2$-G, and (g and h) VO$_2$-cG. (c), (f), and (i) present the simulative structures of VO$_2$-P, VO$_2$-G, and VO$_2$-cG, respectively.

surface, and the monodispersed nano-microspheres had an average diameter of ∼1 μm. The close observation in Fig. 1b revealed that the short and uniform nanoplates with random orientation were formed on the surface of the VO_2-P leading to the obvious roughness. This is a typical coarsening phenomenon caused by Ostwald-ripening (discussed later). With the introduction of GO-ethylene glycol dispersion, the surface of VO_2-G became relatively smooth, and the size of microspheres decreased down to about 0.6-0.8 um (Fig. 1d). Interestingly, the VO_2-G secondary microspheres were constituted by primary nanoparticles rather than nanoplates, and markedly, the resulting microspheres were evenly wrapped by transparent gauze-like rGO (Fig. 1e), which significantly differs from the morphology and structure of the VO_2-P. When the amount of GO-ethylene glycol further increased, a smoother surface of VO_2-G can be created, and the size of VO_2-G drops to ∼0.4 μm (Fig. 1g and h). More importantly, the VO_2 microspheres were uniformly encapsulated by highly crumpled rGO, which is quite consistent with the structural feature reported by Zhao et al. [37]. Note that to realize cG in previous studies is often synthesized by spray-pyrolysis [36], capillary compression [42], and pre-stain relaxation [43], therefore, it is commendable that the facile and rapid wet chemistry synthesis method in this work can easily achieve the above-discussed results, which is superior to the multi-step wet chemistry approach. Additionally, the structural evolution with the function of the dosage of GO-ethylene glycol dispersion was presented in Fig. 1c, f, and i, respectively, to deepen the understanding of their morphologies and structures characterization.

Fig. 2 shows the typical FESEM and EDS mappings of the final sintered powder materials. As shown in Fig. 2a–c, the morphologies and structures of V_2O_5 were virtually identical with those of VO_2 precursors. No obvious changes can be detected after heat treating, indicating that rGO and cG on the surface of V_2O_5 have high mechanical strength. As expected, the gauze-like rGO uniformly wrapped V_2O_5 can be easily found in Fig. 2b. More importantly, highly crumpled reduced graphene oxide encapsulated V_2O_5 constituted a three-dimensional continuous porous network frame structure (Fig. 2c), which may be conducive to improve the mass transfer and promote the structural stability of the desired

electrode material. One can expect that the structure is beneficial of enhancing the power density and/or energy density of the electroactive material [37]. The rGO and V_2O_5 composite structure can be further confirmed in the EDS mappings of all three of the sintered samples in Fig. 2d–f. It can be clearly observed that each of the elemental mappings of V and O manifest the morphologies of their respective bulk materials. No obvious response signal of carbon can be detected in V_2O_5-P (Fig. 2d), while both V_2O_5-G and V_2O_5-cG displayed the highlighted elemental mappings of C, suggesting the sophisticated combination of the synthesized rGO and V_2O_5. Furthermore, as shown in the inset of Fig. 2a–c, the digital photographs of the sintering materials indicated the increasing content of rGO and its relative content due to the color of the as-fabricated material darkening.

To further clarify the structures of the final products, high-resolution TEM was performed on all three of the sintered samples and the results are manifested in Fig. 3. To identify the shell thickness of the obtained microspheres, it is important here to mention that the shell is largely depending on the Ostwald-ripening time in the nanocomposites. More importantly, the Ostwald-ripening is a rapid and thorough process under high temperature pressure (discussed later). Namely, the shell thickness is uniform in comparison to the size distribution of microsphere. As seen in Fig. 3a, V_2O_5-P exhibited a hollow structure including partial yolk-shelled structure, and remarkably, the shell of microspheres was highly uniform with a thickness of about 180 nm (Fig. 3b). In contrast, almost all of the V_2O_5-G microspheres were the single hollow structure, with similar shell thickness of about 100 nm (Fig. 3d and e). Meanwhile, the visible rGO can be easily found on the surface of V_2O_5-G microspheres. More importantly, the relatively thin shell of V_2O_5-G could be the tangible evidence that the gauzy rGO uniformly wrapped on the surface of V_2O_5-G since the rGO as a diffusion barrier for growth substance effectively restrained the coarsening of solvothermal precursor induced by Ostwald-ripening. As for V_2O_5-cG, one can discover that the V_2O_5 microspheres were extreme evenly encapsulated by highly crumpled reduced graphene oxide (Fig. 3g), and the mutual crosslinking rGO constituted the continuous and porous network texture (Fig. 3h), which is consistent with the SEM results.
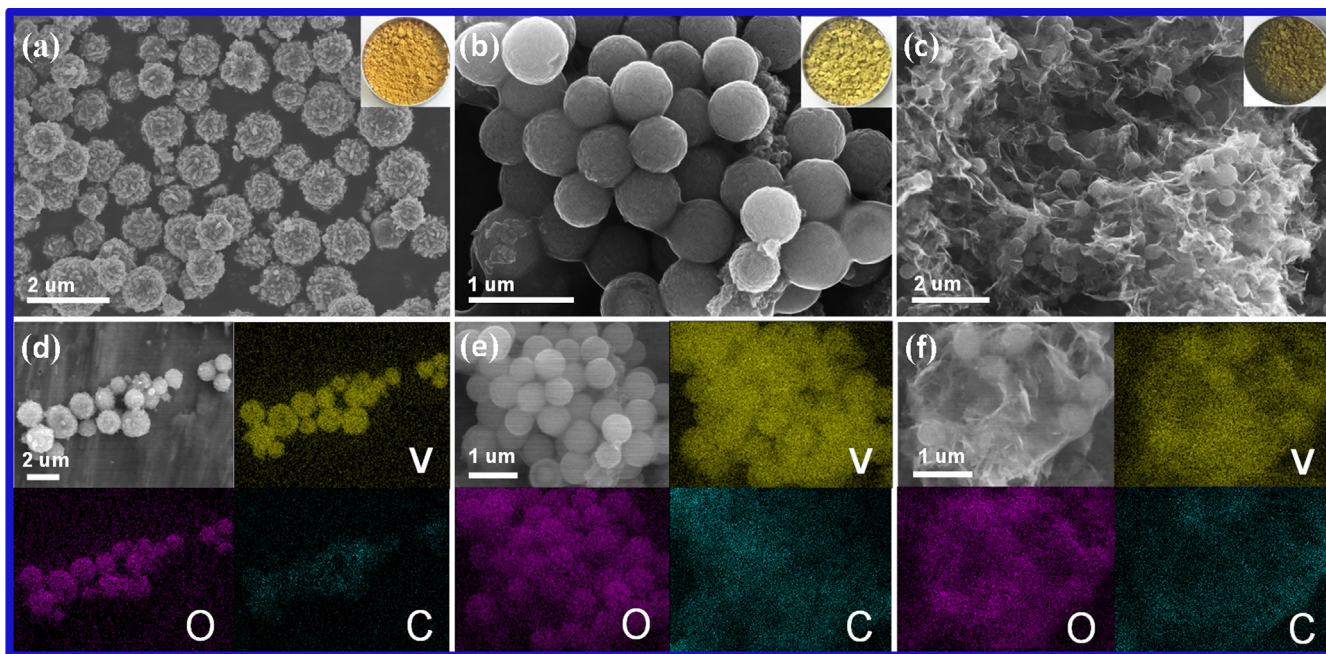

Fig. 2. FESEM images of the sintered products: (a) V_2O_5-P, (b) V_2O_5-G, and (c) V_2O_5-cG. (d–f) show the EDS mappings of V_2O_5-P, V_2O_5-G, and V_2O_5-cG, respectively. Inset of (a–c): the digital photographs of the corresponding products.
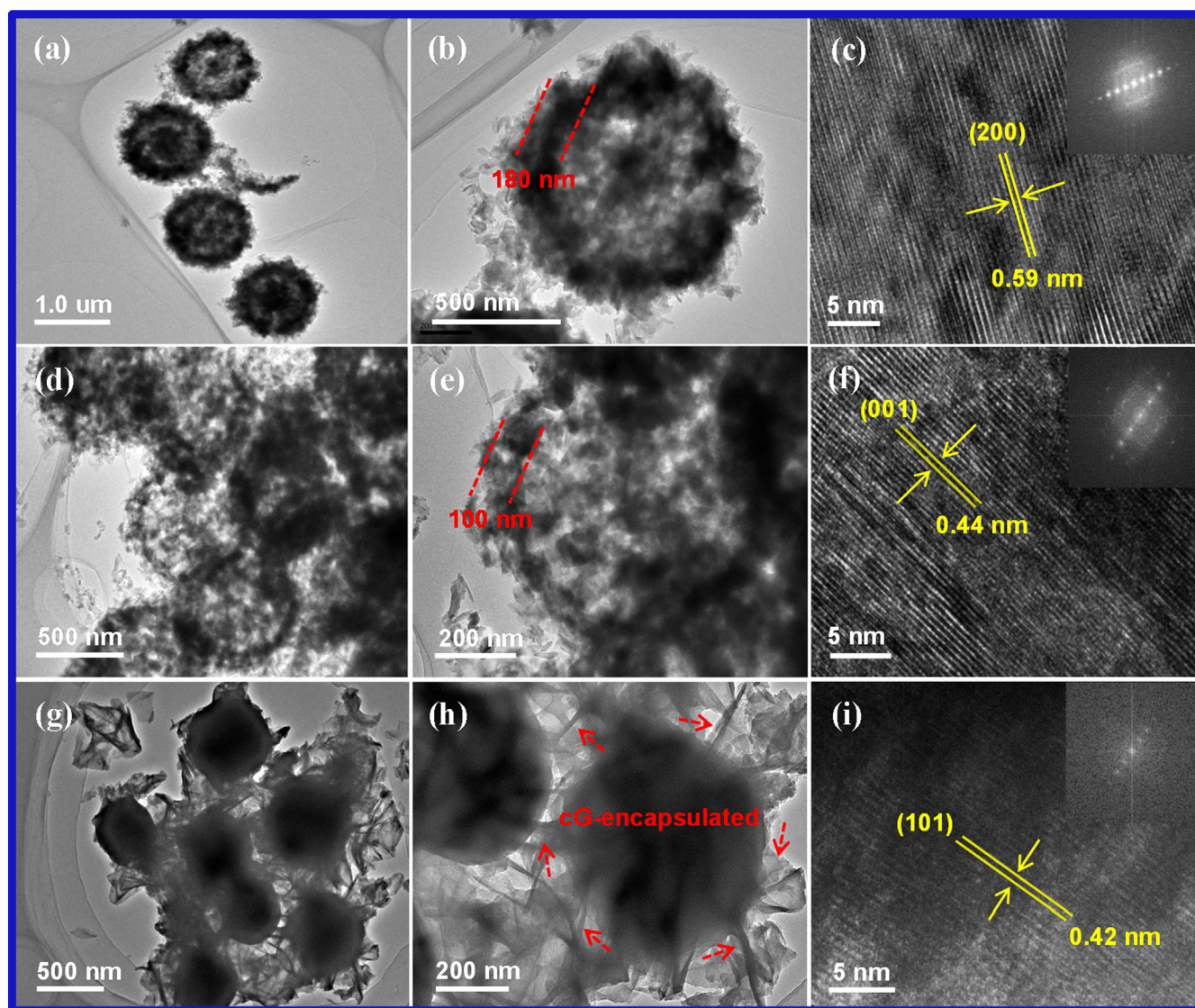
Fig. 3. TEM and high resolution TEM images of the sintered products: (a–c) V_2O_5-P, (d–f) V_2O_5-G, and (g–i) V_2O_5-cG. Inset of (c), (f), and (i): the corresponding fast Fourier-transfer transformation patterns.

Although it was hard to verify the actual structure of the V_2O_5 in V_2O_5-cG owing to the presence of cG, the hollow porous texture of V_2O_5 can be powerfully confirmed by the Supplementary Fig. S2 that shows the TEM images of V_2O_5-cG after oxidizing the rGO by sintering in air at 500 °C for 6 h. Furthermore, as indicated by high-resolution TEM images shown in Fig. 3c, f, and i, the clear lattice spacing of 0.59, 0.44 and 0.42 nm were observed by V_2O_5-P, V_2O_5-G, and V_2O_5-cG, respectively, which were in good agreement with the d-spacing of (200), (001) and (101) facets of the orthorhombic phase V_2O_5 (JCPDS Card no. 41-1426), implying the excellent crystallinity of the obtained sintering samples. Meanwhile, this conclusion can be also proved by the corresponding fast Fourier transformation (FFT) patterns shown in the inset of Fig. 3c, f, and i. The crystalline phase of all three of the final materials was further characterized by XRD. As can be seen from Fig. 4a, all the discernible diffraction peaks can be indexed to the orthorhombic V_2O_5 (lattice parameters $a=11.516$ Å, $b=3.566$ Å, $c=4.373$ Å, Pmmn space group, JCPDS 41-1426), and no obvious impurity peaks can be observed, indicating the obtained V_2O_5 phase with high purity and the complete conversion from VO_2 to V_2O_5 during heat-treatment. Interestingly, the diffraction peak of rGO cannot be detected in Fig. 4a, while FTIR and Raman spectra indeed prove

the existence of composite rGO and V_2O_5. The FTIR spectra (Fig. 4b) displayed that the characteristic peaks of vanadium oxide for V_2O_5-P, V_2O_5-G, and V_2O_5-cG appeared at 1020, 839, 638 and 517 cm^{-1} were corresponding to the stretching vibration of terminal oxygen bonds, the vibration of doubly coordinated oxygen bonds and the asymmetric and symmetric stretching vibrations of triply coordinated oxygen bonds, respectively, which were characteristic modes for V_2O_5 [44,45]. Importantly, the additional bonds located at 1589, 2329, 2359 and 3728 cm^{-1} can be clearly observed for both V_2O_5-G and V_2O_5-cG, which belonged to the skeletal vibration for rGO, suggesting the complete composite of rGO and V_2O_5. This result can also be confirmed from Fig. 4c that shows the Raman spectra of V_2O_5-P, V_2O_5-G, and V_2O_5-cG. Specifically, the discernible peaks centered at 282.4, 304.2, 406.2, 477.9, 527.8, 699.3 and 994.6 were unique bands for V_2O_5, which is quite consistent with previously reported results [36,45]. On the other hand, there were two broad peaks at 1359 and 1604 cm^{-1} in both V_2O_5-G and V_2O_5-cG, corresponding to the D and G bands of rGO [45]. For quantifying the amount of carbon/rGO in the obtained materials, thermogravimetric analysis was carried out in air. The carbon content in the V_2O_5-P, V_2O_5-G, and V_2O_5-cG was evaluated to be about 0.06, 1.31, and 5.01 wt%, respectively (Fig. 4d) [36]. It is
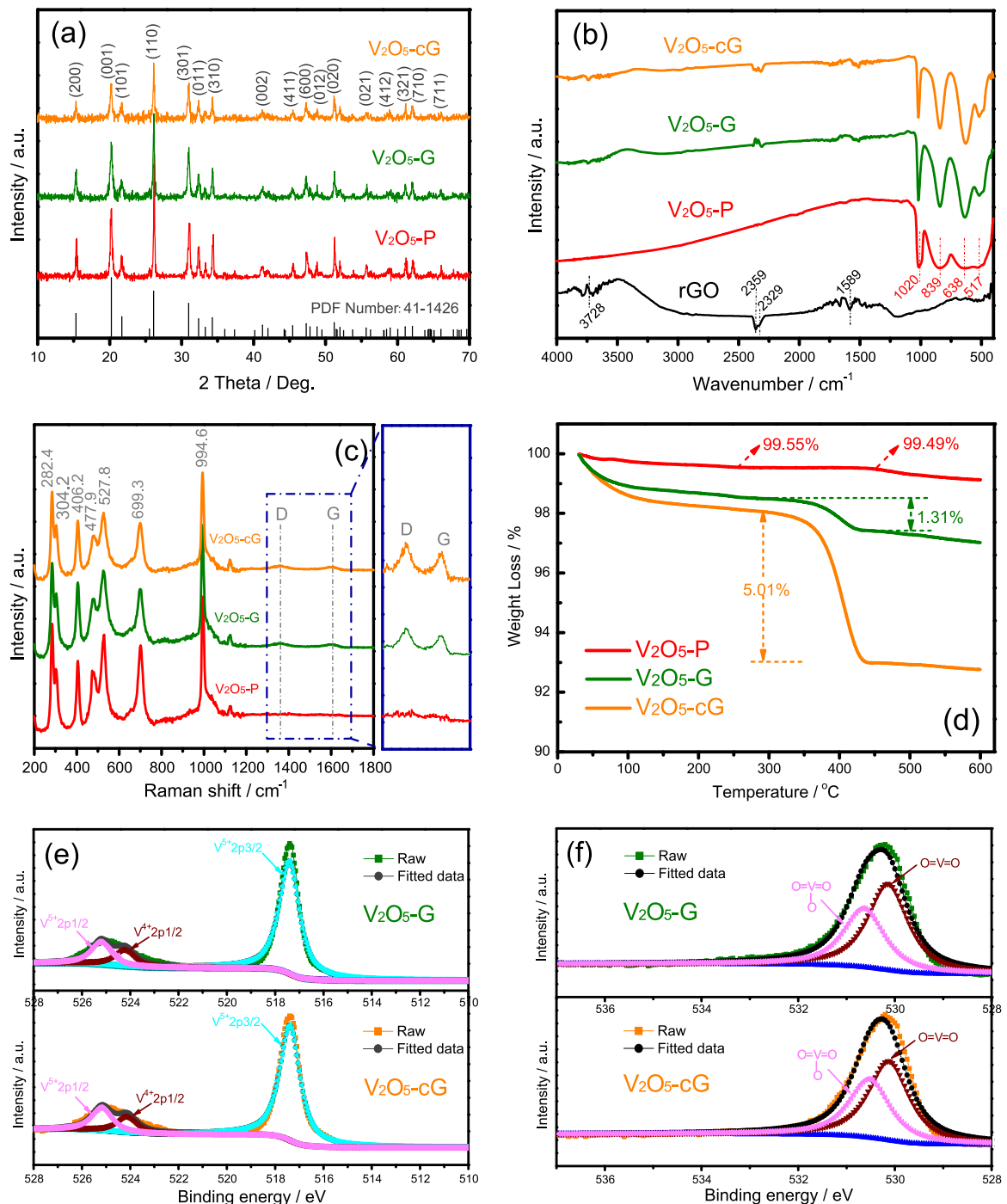
Fig. 4. XRD patterns (a), FTIR spectra (b), Raman spectra (c), and TGA curves (d) of V_2O_5-P, V_2O_5-G, and V_2O_5-cG. XPS of (e) V 2p and (f) O 1s spectra of V_2O_5-G and V_2O_5-cG.

worth mentioning here that the existence of rGO could improve the interfacial and structural stability of the final composite due to the detachable V $2p_{1/2}$, V $2p_{3/2}$, and O 1s core peaks suggesting the partial carbothermal reduction of V^{5+} into V^{4+} (Fig. 4e and f) [45]. However, the difference between interaction of rGO and V_2O_5 in V_2O_5-G and V_2O_5-cG may not exist not only because of the almost overlapping V 2p and O 1s spectra of V_2O_5-G and V_2O_5-cG (see Supplementary Fig. S3), but also because of the almost identical relative molar ratio of V^{5+} to V^{4+} (8.29:1 for V_2O_5-G and 8.69:1 for V_2O_5-cG based on the peak areas).

3.2. Lithium storage performance of the prepared electrodes

To highlight the advantages of the proposed structure, the electrochemical performance of V_2O_5-cG as LIB cathode was systematically evaluated to verify the significant effects of cG, in comparison to the V_2O_5-P and V_2O_5-G electrodes. Fig. 5a–c shows the charge/discharge curves of V_2O_5-P, V_2O_5-G, and V_2O_5-cG at various charge/discharge current densities in the voltage window of 2.0–4.0 V (*vs.* Li/Li$^+$). Clearly, the discharge/charge curves of all three of the electrodes showed visible three plateaus at initial low current density, corresponding to a series of phase transformation during lithium ion intercalation/reintercalation into the V_2O_5 crystal. These results were in accordance with the redox peaks
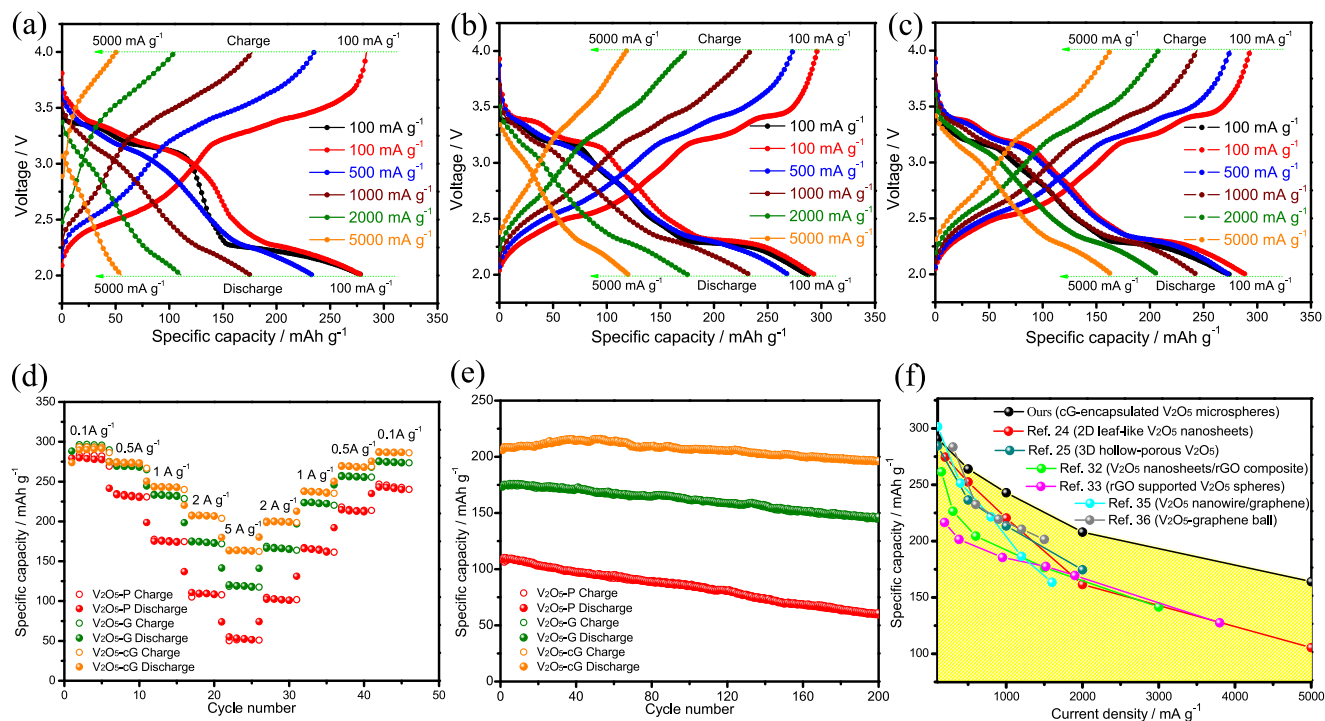
Fig. 5. Charge/discharge curves of (a) V_2O_5-P, (b) V_2O_5-G, and (c) V_2O_5-cG electrodes at various current densities. The black lines correspond to the first discharge curves of the test electrodes at 0.1 A g^{-1}, while the red lines are the second charge/discharge curves of the test electrodes at 0.1 A g^{-1}. (d) Rate performance at various current densities from 0.1 to 5 A g^{-1} for V_2O_5-P, V_2O_5-G, and V_2O_5-cG electrodes. (e) Long-term cycling performance of V_2O_5-P, V_2O_5-G, and V_2O_5-cG electrodes at a current density of 2 A g^{-1}. (f) Comparison of the C-rate results of V_2O_5-cG to other reported V2O5 based electrodes.

shown in the CV profiles (see Supplementary Fig. S4), indicating that the existence of rGO negligibly affects the electrochemical reaction of V_2O_5 with lithium. The discharge capacities for V_2O_5-P were 282, 235, 178, and 110 mA h g^{-1} at the current densities of 100, 500, 1000, and 2000 mA g^{-1}, respectively (Fig. 5a). Meanwhile, a very limited capacity of 51 mA h g^{-1} (corresponding to 153 W h kg^{11} and 3060 W kg^{-1}; Supplementary Fig. S5) was released at a current density of 5000 mA g^{-1}, suggesting a poor rate performance. Conversely, as shown in Fig. 5b and c, the V_2O_5-G and V_2O_5-cG electrodes exhibited significantly improved rate capacities. To be specific, the V_2O_5-G delivered discharge capacities of 293, 273, 234, 175, and 118 mA h g^{-1} at the current densities of 100, 500, 1000, 2000, and 5000 mA g^{-1}, respectively, while the capacities of V_2O_5-cG were more commendable, as correspondingly represented by the values of 291, 274, 243, 208, and 164 mA h g^{-1}. From these observations, therefore, it can be concluded that the introduction of rGO to encapsulate V_2O_5 results in a tremendous influence on the rate capacity of the obtained materials, of which the rate capability of V_2O_5-cG was particularly striking. Note that the power density of V_2O_5-cG increased from 264 W kg^{-1} to 9840 W kg^{-1} (see Supplementary Fig. S5) with the charge/discharge current density increasing from 100 to 5000 mA g^{-1}, which was evidently higher than these of the values for V_2O_5-G and V_2O_5-P. The superior electrochemical performance of V_2O_5-cG can be further confirmed by Fig. 5d that reveals the comparison of rate capability of the obtained V_2O_5-cG as well as the V_2O_5-G and V_2O_5-P electrodes. As shown in Fig. 5d, the V_2O_5-cG displayed the highest rate capacities. More importantly, the reversible capacity of V_2O_5-cG electrode was almost fully recovered after the electrochemical cell worked at various current densities, demonstrating the excellent cycling stability of V_2O_5-cG. In contrast, both V_2O_5-G and V_2O_5-P electrodes showed obvious capacity fade. For example, when the current density returned to 100 mA g^{-1} after 40 cycles, the discharge capacities of V_2O_5-G and V_2O_5-P were 275 and 246 mA h g^{-1}, respectively, while the

corresponding value of V_2O_5-cG can reach as high as 287 mA h g^{-1}. Fig. 5e systematically compares the long-term charge/discharge cycling for all three of the electrodes at the current density of 2000 mA g^{-1}. In Fig. 5e, it can be seen that the V_2O_5-P electrode exhibited a capacity of 61 mA h g^{-1} with the relatively low capacity retention of 56% after 200 cycles, which was far below the corresponding value of 147 mA h g^{-1} for V_2O_5-G with a high capacity retention of 84%. More remarkably, the V_2O_5-cG electrode displayed a different cycling behavior when compared with both V_2O_5-G and V_2O_5-P electrodes. Specifically, the discharge capacity of V_2O_5-cG increased after the first eight cycles, and reached a maximum of 216 mA h g^{-1} in the 51th cycle, suggesting that the electroactive material of V_2O_5-cG electrode is gradually activated stemming from the penetration of organic electrolyte restricted by thicker rGO as well as the relatively low crystallinity of V_2O_5 [46–48]. Furthermore, after 200 cycles, a discharge capacity of 196 mA h g^{-1} was retained, corresponding to the capacity retention of 94% and to the capacity fading of 0.03% per cycle. From the above results it can be concluded that V_2O_5 encapsulated by cG results in excellent rate capability and prominent cycling stability for Li$^+$ storage. Meanwhile, these performance improvements can be mainly attributed to several factors, as follows: (i) the improved electronic conductivity due to the formation of superior conductive network by cross-linked cG [29,32,37]; (ii) the enhanced electrochemical activity, structural stability and strain tolerability because of the nanoporous structure of V_2O_5-cG [24,25,32,33]; (iii) the preventing vanadium dissolution owing to the organic electrolyte physically separated by cG [17]; (iv) the decreasing charge transfer resistance originating from the enhanced electrolyte wettability of the working electrode by cG [24,29,37]. The lithiation process of the as-synthesized V_2O_5-based electrodes was diagrammatized in the Fig. 6 [37,49], which can be fully supported by the SEM images of cycled electrodes (see Supplementary Fig. S6). Specifically, one can clearly observe the macroporous and fractured electroactive material of
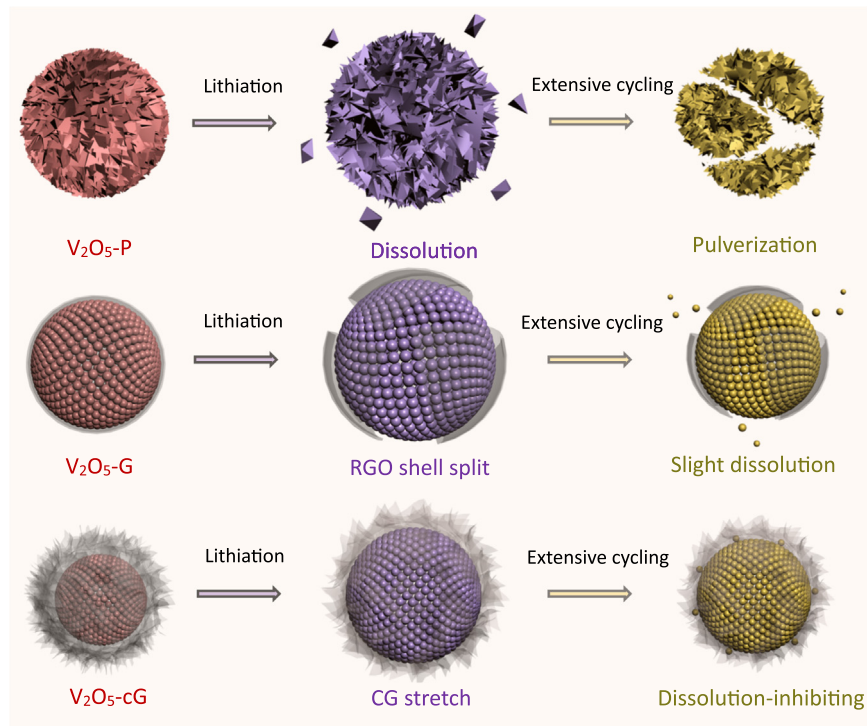
Fig. 6. Schematic illustration of the lithiation processes of V_2O_5-P, V_2O_5-G, and V_2O_5-cG electrodes.

V_2O_5-P due to the potential dissolution and stress effect in Fig. S6a, while the morphological structure of V_2O_5-cG almost remains relatively unchanged as shown in Fig. S6b. Importantly, these observations confirm that the V_2O_5-cG material possesses a significantly structural advantage over other two samples. Here, to further confirm the advantages of the resultant V_2O_5-cG electrode, Fig. 5f provides the comparison of the rate capability of the designed V_2O_5-cG and other reported V_2O_5 based electrodes. It is clear that the rate performance of our desired V_2O_5-cG may be better than those of nanostructured V_2O_5 electrodes reported

previously, including leaf-like V_2O_5 nanosheets [24], hollow-porous V_2O_5 microspheres [25], and other V_2O_5-graphene based nanocomposites [32,33,35,36].

In order to further illustrate the electrochemical performance of all three of the obtained materials, we carried out electrochemical impedance spectroscopy (EIS) to study the electrochemical reaction kinetics and analyze the variation of electrode/electrolyte interface involving during charge/discharge cycles. Fig. 7a–c shows the EIS spectra of the V_2O_5-P, V_2O_5-G, and V_2O_5-cG electrodes at full-discharged state after different cycles,
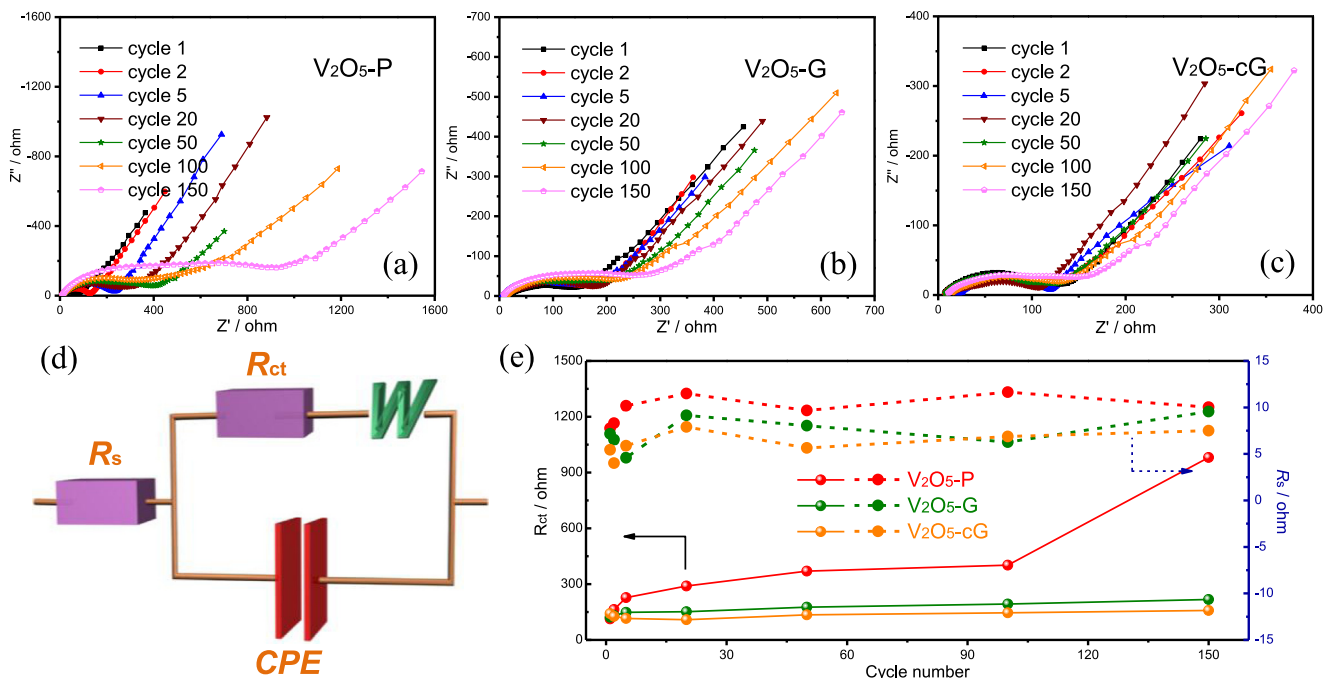

Fig. 7. Nyquist plots of (a) V_2O_5-P, (b) V_2O_5-G, and (c) V_2O_5-cG electrodes at full-discharged state after various cycles. (d) Equivalent circuit used to simulate the EIS in this study. (e) EIS parameters of V_2O_5-P, V_2O_5-G, and V_2O_5-cG electrodes derived from the equivalent circuit.

respectively. Note that no obvious surface film semicircles can be found in all the Nyquist plots, which is consistent with the stable potential window of the organic liquid electrolyte. Namely, all the spectra displayed two well-defined regions of a depressed semi-circle in the high-frequency region and a sloped line in the low-frequency region. Therefore, the equivalent circuit employed to simulate the kinetics parameters can be expressed as shown in Fig. 7d. In the equivalent circuit, R_s represents the ohmic resistance of whole reaction system; R_{ct} stands for charge transfer resistance between the electrode and the electrolyte; CPE is the double layer capacitance on the electrode surface; and W is the Warburg impedance associated with solid state diffusion. It is noticeable that the constant phase element (CPE) was employed in the equivalent circuits instead of pure capacitance owing to the inhomogeneous surface of the working electrode [50,51]. Based on the equivalent circuits, the obtained kinetics parameters are summarized in Fig. 7e. Overall, the average R_s value for V_2O_5-P, V_2O_5-G, and V_2O_5-cG electrodes was gradually reduced in sequence. This is expected to happen if we consider the carbon relative content in V_2O_5-P, V_2O_5-G, and V_2O_5-cG. Furthermore, the continuous change in R_s implied the variation of electrode structure and/or electrode/electrolyte interface, which may be closely related to the contact between the electroactive particles [51]. The steady increase of R_{ct} of V_2O_5-P from 113 Ω to 980 Ω upon the charge/discharge cycles revealed that the electrochemical reaction became much more difficult with the increase of the cycling number. This result co-ordinates with the capacity fade of V_2O_5-P at the current density of 2000 mA g^{-1} (Fig. 6e). When there was a small amount of rGO to combine with V_2O_5, the increasing trend of R_{ct} decreased. For example, the V_2O_5-G displayed the relatively low values of R_{ct}, the R_{ct} value only increased from 122 Ω (the 1st cycle) to 217 Ω (the 150th cycle), indicating the improved electrochemical performance (Fig. 6d and e). Interestingly, the R_{ct} value of V_2O_5-cG initially decreased from 141.6 Ω (the 1st cycle) to 108 Ω (the 20th cycle), and then slightly increased to 158 Ω (the 150th cycle). Such an abnormal variation of R_{ct} further confirmed the V_2O_5-cG electrode experienced a slow activation process. To be specific, V_2O_5-P with rough surface reveals a large and sufficient contact area with organic electrolyte, and thus the charge transfer across V_2O_5-P electrode/electrolyte interface may be much easier viz. the lowest R_{ct} value in the first cycle. As for V_2O_5-cG, the contact area of electrode/electrolyte is restricted by the existence of thick rGO layer, and therefore, the initial decrease of R_{ct} may be associated with the penetration effect of organic electrolyte. In other words, the electroactive material of V_2O_5-cG electrode is gradually activated with the sufficient penetration of organic electrolyte. On the

other hand, as previously reported [46–48], the difference in crystallinity of these materials may be another possible reason causing this activation process. It is worth mentioning here that the R_{ct} value of V_2O_5-cG in the whole cycle process was obviously lower than those values of V_2O_5-P and V_2O_5-G, implying that the V_2O_5-cG electrode possessed the smallest electrochemical reaction polarization, viz., the optimal rate capability. In short, all these results clearly illuminate the electrochemical performance evolution of the obtained electrodes, which in turn provide the valuable information to search the effective strategies further optimizing the performance of the target products.

3.3. Structural evolution and formation mechanism

On the basis of the aforementioned discussions, it should be noted that the essential structures of all three of the final materials had already formed during the solvothermal treatment. It is more reasonable to focus on the structural evolution of precursors for illuminating the formation mechanism. Fig. 8a schematically illustrates the time-dependent intrinsic structural evolution of VO_2-P. Briefly, the fresh stable VO_2 nucleus are first generated in the supersaturated butanol solution due to the continuous hydrolysis of VOC_2O_4 ($2VOC_2O_4 \rightarrow 2VO_2 + 3CO_2 + C$) [11,41]. Then, the growing VO_2 monomers undergo the aggregation process, and transform to nano-microspheres to reduce overall surface free energy in stage I [11,52]. With extended solvothermal process, as shown in stage II, the exterior of the clustered microspheres continue to grow up at the expense of the dissolution of the interior nucleus and gradually engender the yolk-shelled structure, which is also known as the Ostwald-ripening process [11,53,54]. Finally, completely hollow microspheres are obtained as a result of the thorough dissolution and re-crystallization of the less stable interior architectures (stage III). This is consistent with the SEM and TEM images of V_2O_5-P (Figs. 2a and 3a). In addition, this growth mechanism can be fully supported by the SEM images of VO_2-P precursors obtained at different solvthermal time (see Supplementary Fig. S7). The VO_2 nano-microspheres collected after solvthermal reaction of 1 h display a relatively smooth surface due to the relatively short period of ripening time. Meanwhile, the existence of the cracked solid hemisphere of VO_2 suggests the subsistent aggregation process of the growing VO_2 monomers. Undoubtedly, all these observations match well with the proposed structural evolution. With further prolonging the reaction time from 4 h to 16 h, the morphologies of VO_2 nano-microspheres hardly changed. This implies that the Ostwald-ripening is a rapid and thorough process under high temperature
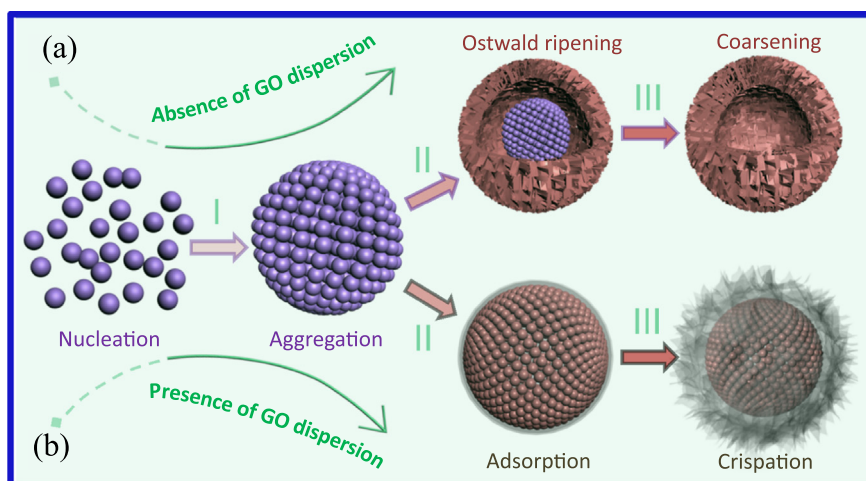

Fig. 8. Time-dependent intrinsic structural evolution of (a) pure VO_2 and (b) rGO encapsulated VO_2.

pressure. Interestingly, the structural evolution of VO$_2$ precursors was significantly affected due to the presence of the GO-ethylene glycol dispersion in the solvothermal system. As shown in stage II of Fig. 8b, the graphene oxide (GO) in the reaction system can be effectively reduced and uniformly deposited on the surface of VO$_2$ microspheres, which can be attributed to the following two reasons: (i) the rGO and decomposition product of VOC$_2$O$_4$ are adequately mixed under high pressure condition of solvothermal reactions; (ii) the combining effects of both electrostatic attraction and overall surface energies facilitate the conformal deposition of rGO on the surface of VO$_2$ microspheres [37,52]. In fact, the even dispersion of graphene sheets onto the VO$_2$ microspheres can be clearly observed in Figs. 1 and 2. With the limited amount of GO dispersion, the conglobate VO$_2$ was only wrapped by the thin layer of the gauze-like rGO (i.e. VO$_2$-G). When the additive GO dispersion further increased, however, the stack and crimp processes
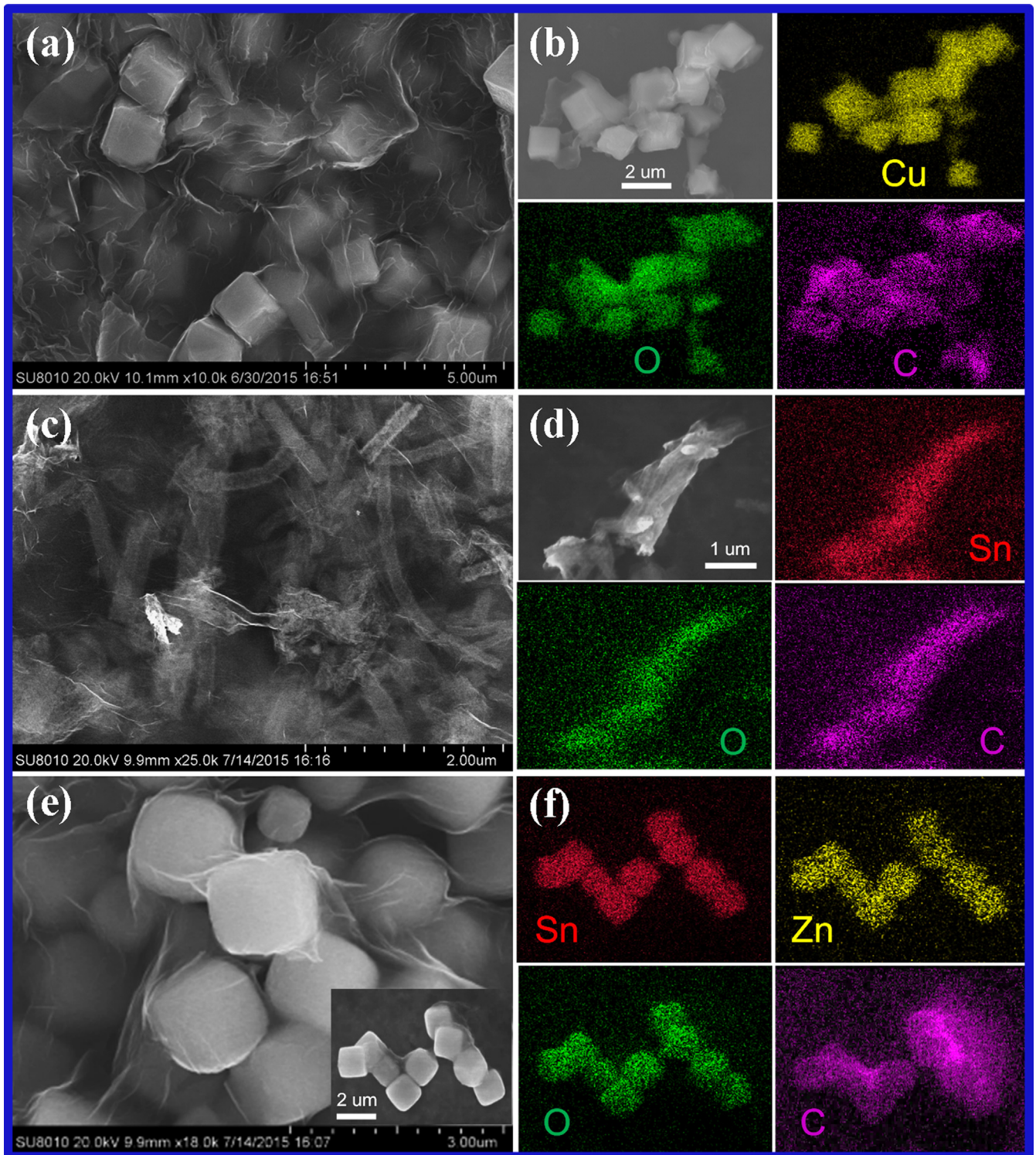

Fig. 9. Crumpled reduced graphene oxide encapsulated (a) CuO microcubes, (c)SnO$_2$ nanotubes, and (e) Zn$_2$SnO$_4$ boxes. Energy dispersive spectroscopy (EDS) elemental mappings of crumpled reduced graphene oxide encapsulated (b) CuO microcubes, (d) SnO$_2$ nanotubes, and (f) Zn$_2$SnO$_4$ boxes.

inevitably occurred in the subsequent accretion of rGO to maintain the thermodynamic stability for the final product (stage III in Fig. 8b). Interestingly, the rGO as a diffusion barrier for growth can effectively restrain the surface coarsening of VO_2 precursor induced by Ostwald-ripening, which greatly reduced the surface roughness of both VO_2-G and VO_2-cG. Meanwhile, the nuclear dissolution of VO_2 microspheres caused by inside-out Ostwald-ripening can easily induce the secondary recrystallization. One can readily detect this phenomenon from the SEM images of VO_2-G and V_2O_5-G (Figs. 1d and 2b). Furthermore, to further clarify the formation mechanism, GO deionized water/butanol suspension (2 mg mL^{-1}) was employed to replace the GO ethylene glycol suspension to fabricate the rGO/VO_2 nanocomposite. It can be observed that the morphologies and sizes of the obtained VO_2 microspheres have been significantly changed (see Supplementary Fig. S8). More notably, the reduced graphene oxide had failed to encapsulate or conformally wrap around the VO_2 microspheres. Conversely, if the butanol solvent was substituted with deionized water or ethylene glycol, the morphologies of the final product change completely (see Supplementary Fig. S9). From these observations, therefore, it can be concluded that both the butanol solvent and GO-ethylene glycol suspension were the key ingredients to guarantee the cG uniform coating or conformal covering of the VO_2 microspheres, and essentially, this may be associated with the polarity and viscosity of the proposed unique solvent system. If this conclusion was an established fact, in other words, the proposed reaction system not only can realize the *in-situ* encapsulation of the newborn nanoparticles via this solvent system like the aforementioned VO_2 nano-microspheres, but also effectively encapsulate the extrinsic solid powders. Inspired by this idea, we attempted to encapsulate multi-element compounds typically including solid CuO microcubes (Fig. S10a), porous SnO_2 nanotubes (Fig. S10b), and hollow Zn_2SnO_4 boxes (Fig. S10c). As expected, a series of cG-encapsulated M (M=CuO, SnO_2, Zn_2SnO_4) had been successfully synthesized using the proposed reaction system of butanol solvent and GO-ethylene glycol dispersion (Fig. 9a, c, and e). Meanwhile, the corresponding EDS mappings shown in Fig. 9b, d, and f indeed confirm the employed materials conformally encapsulated by transparent gauze-like cG. Interestingly, the nickel sulfide nanobundle arrays on nickel foam can be also coated by cG via this extensible reaction system (see Supplementary Fig. S11), further highlighting the versatility of this method. All these observations demonstrated the success of the designed approach as well as its promising application with high scalability. Undoubtedly, such finding provides an effective shortcut to construct crumpled graphene based functional materials for the multitudinous application domains.

4. Conclusions

In this paper, we have successfully synthesized the crumpled reduced graphene oxide encapsulated porous V_2O_5 nano/microspheres via a facile and scalable approach. The conformally wrapped cG has a profound influence on the lithium storage performance of V_2O_5, deriving from the simultaneous improvements in electronic conductivity, structural stability, and charge transfer resistance. This V_2O_5-cG electrode with only 5 wt. % rGO can deliver a reversible capacities as high as 163 mA h g^{-1} at 5 A g^{-1} corresponding to 492 W h kg^{-1} and 9840 W kg^{-1}, and the capacity retention of about 94% after 200 cycles at 2000 mA g^{-1} in the potential range between 2.0 V and 4.0 V (*vs.* Li/Li$^+$). These values are significantly better than those of the reported nanostructured V_2O_5 electrodes. Undoubtedly, this is a quite valuable example that the performance of the electrode materials is strongly rooted in the structural configuration of electroactive

material. Furthermore, a series of multi-element compound materials had been successfully encapsulated using this versatile method, further highlighting the fascination of the proposed reaction system. It is expected that such finding will provide an effective method to construct crumpled graphene based functional materials, and open up the application spree of this kind of functional materials.

Acknowledgments

Appendix A. Supporting information

Supplementary data associated with this article can be found in the online version at http://dx.doi.org/10.1016/j.nanoen.2016.04.002.

References

[1] J.M. Tarascon, M. Armand, Nature 414 (2001) 359–367.
[2] C. Yuan, H. Wu, Y. Xie, X. Lou, Angew. Chem. Int. Ed. 53 (2014) 1488–1504.
[3] R.V. Noorden, Nature 507 (2014) 26–28.
[4] J. Jiang, Y. Li, J. Liu, X. Huang, C. Yuan, X. Lou, Adv. Mater. 24 (2012) 5166–5180.
[5] T.H. Kim, J.S. Park, S.K. Chang, S. Choi, J.H. Ryu, H.K. Song, Adv. Energy Mater. 2 (2012) 860–872.
[6] N.S. Choi, Z. Chen, S.A. Freunberger, X. Ji, Y.K. Sun, K. Amine, G. Yushin, L. F. Nazar, J. Cho, P.G. Bruce, Angew. Chem. Int. Ed. 51 (2012) 9994–10024.
[7] S. Wang, S. Li, Y. Sun, X. Feng, C. Chen, Energy Environ. Sci. 4 (2011) 2854–2857.
[8] H. Wang, D. Ma, Y. Huang, X. Zhang, Chem. Eur. J. 18 (2012) 8987–8993.
[9] S. Zhou, X. Yang, Y. Lin, J. Xie, D. Wang, ACS Nano 6 (2012) 919–924.
[10] Y. Liu, M. Clark, Q. Zhang, D. Yu, D. Liu, J. Liu, G. Cao, Adv. Energy Mater. 1 (2011) 194–202.
[11] A. Pan, H. Wu, L. Yu, X. Lou, Angew. Chem. 125 (2013) 2282–2286.
[12] C. Delmas, H.C. Auradou, J.M. Cocciantelli, M. Menetrier, J.P. Doumerc, Solid State Ion. 69 (1994) 257–264.
[13] J.M. Cocciantelli, M. Menetrier, C. Delmas, J.P. Doumerc, M. Pouchard, M. Broussely, J. Labat, Solid State Ion. 78 (1995) 143–150.
[14] A.D. Pasquier, C. Huang, T. Spitler, J. Power Sources 186 (2009) 508–514.
[15] Y. Jang, B. Huang, Y. Chiang, D.R. Sadoway, Electrochem. Solid State Lett. 1 (1998) 13–16.
[16] L. Hu, F. Wu, C. Lin, A.N. Khlobystov, L. Li, Nat. Commun. 4 (2013) 1687.
[17] X. Sun, C. Zhou, M. Xie, T. Hu, H. Sun, G. Xin, G. Wang, S.M. George, J. Lian, Chem. Commun. 50 (2014) 10703–10706.
[18] Z. Li, H. Zhang, Q. Liu, Y. Liu, L. Stanciu, J. Xie, ACS Appl. Mater. Interfaces 6 (2014) 18894–18900.
[19] H. Yu, X. Rui, H. Tan, J. Chen, X. Huang, C. Xu, W. Liu, D.Y.W. Yu, H.H. Hng, H. E. Hoster, Q. Yan, Nanoscale 5 (2013) 4937–4943.
[20] Y. Wang, K. Takahashi, K.H. Lee, G. Cao, Adv. Funct. Mater. 16 (2006) 1133–1144.
[21] Y. Wang, G. Cao, Chem. Mater. 18 (2006) 2787–2804.
[22] B. Yan, X. Li, Z. Bai, M. Li, L. Dong, D. Xiong, D. Li, J. Alloy. Compd. 634 (2015) 50–57.
[23] B. Li, Y. Xu, G. Rong, M. Jing, Y. Xie, Nanotechnology 17 (2006) 2560–2566.
[24] Y. Li, J. Yao, E. Uchaker, J. Yang, Y. Huang, M. Zhang, G. Cao, Adv. Energy Mater. 3 (2013) 1171–1175.
[25] L. Mai, Q. An, Q. Wei, J. Fei, P. Zhang, X. Xu, Y. Zhao, M. Yan, W. Wen, L. Xu, Small 10 (2014) 3032–3037.
[26] Y. Hu, X. Liu, J.O. Müller, R. Schlögl, J. Maier, D. Su, Angew. Chem. Int. Ed. 48 (2009) 210–214.
[27] L. Mai, F. Dong, X. Xu, Y. Luo, Q. An, Y. Zhao, J. Pan, J. Yang, Nano Lett. 13 (2013) 740–745.
[28] J.W. Lee, S.Y. Lim, H.M. Jeong, T.H. Hwang, J.K. Kang, J.W. Choi, Energy Environ. Sci. 5 (2012) 9889–9894.
[29] Q. Liu, Z. Li, Y. Liu, H. Zhang, Y. Ren, C. Sun, W. Lu, Y. Zhou, L. Stanciu, E.A. Stach, J. Xie, Nat. Commun. 6 (2015) 6127.
[30] A. Fasolino, J.H. Los, M.I. Katsnelson, Nat. Mater. 6 (2007) 858–861.

[31] K. Zhang, J.T. Lee, P. Li, B. Kang, J.H. Kim, G. Yi, J.H. Park, Nano Lett. 15 (2015) 6756–6763.
[32] J. Cheng, B. Wang, H. Xin, G. Yang, H. Cai, F. Nie, H. Huang, J. Mater. Chem. A 1 (2013) 10814–10820.
[33] X. Rui, J. Zhu, D.H. Sim, C. Xu, Y. Zeng, H.H. Hng, T.M. Lim, Q.Y. Yan, Nanoscale 3 (2011) 4752–4758.
[34] X. Pan, G. Ren, M.N.F. Hoque, S. Bayne, K. Zhu, Z. Fan, Adv. Mater. Interfaces 1 (2014) 1400398–1400416.
[35] H. Liu, W. Yang, Energy Environ. Sci. 4 (2011) 4000–4008.
[36] S.H. Choi, Y.C. Kang, Chem. Eur. J 20 (2014) 6294–6299.
[37] Y. Zhao, J. Feng, X. Liu, F. Wang, L. Wang, C. Shi, L. Huang, X. Feng, X. Chen, L. Xu, M. Yan, Q. Zhang, X. Bai, H. Wu, L. Mai, Nat. Commun. 5 (2014) 4565.
[38] L. Jiang, Z. Fan, Nanoscale 6 (2013) 1922–1945.
[39] R. Raccichini, A. Varzi, S. Passerini, B. Scrosati, Nat. Mater. 14 (2015) 271–279.
[40] X. Li, Y. Hu, J. Liu, A. Lushington, R. Li, X. Sun, Nanoscale 5 (2013) 12607–12615.
[41] D. Chao, C. Zhu, X. Xia, J. Liu, X. Zhang, J. Wang, P. Liang, J. Lin, H. Zhang, Z. Shen, H. Fan, Nano Lett. 15 (2015) 565–573.
[42] Y. Chen, F. Guo, A. Jachak, S.P. Kim, D. Datta, J. Liu, I. Kulaots, C. Vaslet, H. D. Jang, J. Huang, A. Kane, V.B. Shenoy, R.H. Hurt, Nano Lett. 12 (2012) 1996–2002.
[43] J. Luo, H. Jang, T. Sun, L. Xiao, Z. He, A.P. Katsoulidis, M.G. Kanatzidis, J. M. Gibson, J. Huang, ACS Nano 5 (2011) 8943–8949.
[44] X. Zhou, G. Wu, J. Wu, H. Yang, J. Wang, G. Gao, R. Cai, Q. Yan, J. Mater. Chem. A 1 (2013) 15459–15468.
[45] M. Li, G. Sun, P. Yin, C. Ruan, K. Ai, ACS Appl. Mater. Interfaces 5 (2013) 11462–11470.
[46] D. Liu, Y. Liu, B.B. Garcia, Q. Zhang, A. Pan, Y. Jeong, G. Cao, J. Mater. Chem. 19 (2009) 8789–8795.
[47] X. Wang, Z. Wang, L. Chen, J. Power Sources 242 (2013) 65–69.
[48] E. Kazyak, K.N. Wood, N.P. Dasgupta, Chem. Mater. 27 (2015) 6457–6462.
[49] J. Liu, P. Kopold, C. Wu, P.A. van Aken, J. Maier, Y. Yu, Energy Environ. Sci. 8 (2015) 3531–3538.
[50] A. Sakunthala, M.V. Reddy, S. Selvasekarapandian, B.V.R. Chowdari, P.C. Selvin, Energy Environ. Sci. 4 (2011) 1712–1725.
[51] B. Yan, M. Li, X. Li, Z. Bai, L. Dong, D. Li, Electrochim. Acta 164 (2015) 55–61.
[52] Z. Zhuang, Q. Peng, Y. Li, Chem. Soc. Rev. 40 (2011) 5492–5513.
[53] X. Cao, L. Gu, L. Zhuge, W. Gao, W. Wang, S. Wu, Adv. Funct. Mater. 16 (2006) 896–902.
[54] J. Yu, H. Guo, S.A. Davis, S. Mann, Adv. Funct. Mater. 16 (2006) 2035–2041.

Yang Zhao is currently a Ph.D. candidate in Prof. Xueliang (Andy) Sun's Nanomaterials and Energy Group at the University of Western Ontario, Canada. He received his B.S. degree and M.S. degree in Chemical Engineering and Technology from Northwestern Polytechnical University (Xi'an, China) in 2011 and 2014, respectively. His current research interests focus on atomic layer deposition in the application of lithium/sodium ion batteries and all solid state batteries.

Lei Dong is currently a laboratory technician in Tianjin International Joint Research Center of Surface Technology for Energy Storage Materials at Tianjin Normal University, China. He received his B.S. degree and M.S. degree in Chemical Engineering and Technology from Tianjin Normal University (Tianjin, China) in 2009 and 2014, respectively. His current research interests focus on PECVD&ALD in the application of sodium ion batteries.

Xiaosheng Song received his M.S. degree from Tianjin Normal University in 2015. He is currently a Ph.D. student it the School of Materials Science and Technology at China University of Geosciences (Beijing) under the supervision of Prof. Zhimin Bai and Xifei Li. His current research interests focus on the design of high performance electrode materials and their applications in lithium/sodium ion batteries.

Dejun Li is currently a full professor at Tianjin Normal University. He obtained his Ph.D. at Tsinghua University in 1999. He then worked three years as a postdoctoral follow at Northwestern University of USA. Since 1999 he has been focusing on various thin films, coatings, and nano materials for protection, energy storage and conversion. His research group is currently working on design, synthesis, and applications of various coatings for surface modification of the electrodes of various high performance batteries and supercapacitors as well as tools. He has authored and co-authored over 150 refereed journal articles and 11 patents.

Craig Langford is a graduate student in the Mechanical & Materials Engineering Department at the University of Western Ontario under the supervision of Prof. Xueliang (Andy) Sun. He received his BASc in Nanotechnology Engineering at the University of Waterloo in 2013. His current work focuses on the use of thin films created via atomic and molecular layer deposition on lithium-ion batteries.

Bo Yan is currently a Ph.D. candidate in the School of Materials Science and Technology at China University of Geosciences (Beijing). He received his B.E. (2011) and M.E. (2014) degree from the College of Chemistry and Bioengineering at Guilin University of Technology (Guilin, China). His research interests include the controllable preparation of micro/nanostructures and their applications in lithium/sodium ion batteries and lithium–sulfur batteries.

Dr. Xifei Li is currently a full professor and associate dean of College of Physics and Materials Science at Tianjin Normal University. Since 2001 he has been focusing on various materials for energy storage and conversion. Prof. Li's research group is currently working on design, synthesis as well as performance improvement of the anodes and the cathodes with various structures for high performance lithium ion batteries, lithium sulfur batteries, sodium ion batteries, and supercapacitors. He has authored and co-authored over 100 refereed journal articles, two invited book chapters as well as 13 patents.

Zhimin Bai received his B.E. degree in geology from Hebei University of Geosciences in 1982. He received his M.S. and Ph.D. degree in materials science from China University of Geosciences in 1985 and 2000, respectively. He is currently a professor at school of Materials Science and Technology of China University of Geosciences (Beijing). His current research direction focuses on the comprehensive utilization of minerals and silicate solid waste, and tribological properties of layer silicate minerals.

Professor Xueliang (Andy) Sun is a Senior Canada Research Chair (Tier 1) and Full Professor at the University of Western Ontario, Canada. Dr Sun received his Ph.D. in 1999 at the University of Manchester, UK, which he followed up by working as a postdoctoral fellow at the University of British Columbia, Canada and as a Research Associate at l'Institut national de la recherche scientifique (INRS), Canada. His current research interests are associated with advanced materials for electrochemical energy storage and conversion, including electrocatalysis and catalyst support in fuel cells and electrodes in lithium-ion batteries and metal-air batteries.